ACS APPLIED MATERIALS & INTERFACES

www.acsami.org

Research Article

In Situ Nanocoating on Porous Pyrolyzed Paper Enables Antibiofouling and Sensitive Electrochemical Analyses in Biological Fluids

Caroline Y. N. Nicoliche, Aline M. Pascon, Ítalo R. S. Bezerra, Ana C. H. de Castro, Gabriel R. Martos, Jefferson Bettini, Wendel A. Alves, Murilo Santhiago,* and Renato S. Lima*

Cite This: *ACS Appl. Mater. Interfaces* 2022, 14, 2522−2533

Read Online

ACCESS | Metrics & More | Article Recommendations | Supporting Information

ABSTRACT: Electrochemical detection in complex biofluids is a long-standing challenge as electrode biofouling hampers its sensing performance and commercial translation. To overcome this drawback, pyrolyzed paper as porous electrode coupled with the drop casting of an off-the-shelf polysorbate, that is, Tween 20 (T20), is described here by taking advantage of the *in situ* formation of a hydrophilic nanocoating (2 nm layer of T20). The latter prevents biofouling while providing the capillarity of samples through paper pores, leveraging redox reactions across both only partially fouled and fresh electrodic surfaces with increasing detection areas. The nanometric thickness of this blocking layer is also essential by not significantly impairing the electron-transfer kinetics. These phenomena behave synergistically to enhance the sensibility that further increases over long-term exposures (4 h) in biological fluids. While the state-of-the-art antibiofouling strategies compromise the sensibility, this approach leads to peak currents that are up to 12.5-fold higher than the original currents after 1 h exposure to unprocessed human plasma. Label-free impedimetric immunoassays through modular bioconjugation by directly anchoring spike protein on gold nanoparticles are also allowed, as demonstrated for the COVID-19 screening of patient sera. The scalability and simplicity of the platform combined with its unique ability to operate in biofluids with enhanced sensibility provide the generation of promising biosensing technologies toward real-world applications in point-of-care diagnostics, mass testing, and in-home monitoring of chronic diseases.

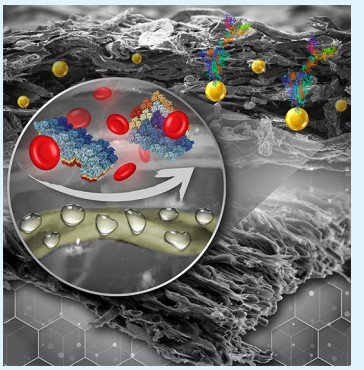

KEYWORDS: *biosensor, complex sample, SARS-CoV-2, COVID-19, point of care*

1. INTRODUCTION

The development of commercially feasible platforms for point-of-care (POC) diagnostics has emerged as a frontier and valuable challenge in the bio-/sensing field.[1,2] Such platforms should be able to provide user-friendly and rapid analyses through a cost-effective, handheld, and scalable setting. While electrochemical devices can meet the demands for developing field-deployable setups with high sensibility and selectivity,[1−9] they have failed in translating useful solutions for many biomarkers other than glucose into the real world.[2] The major obstacle that hinders the commercial translation of electrochemical biosensors is biofouling, that is, the nonspecific adsorption of proteins at the electrode surface when exposed to bodily fluids such as blood plasma and serum.[10,11] Originating from electrostatic and hydrophobic interactions, biofouling blocks electron transfer, thus compromising the detection performance in terms of sensibility, selectivity, accuracy, and reproducibility.[12−14]

The strategies to circumvent biofouling include self-assembled monolayers of polyethylene glycol,[15] zwitterionic polymers,[16−18] hybrid coating,[10] and bovine serum albumin (BSA).[19] Although valuable, these layers are usually detrimental to the detection performance as they create high-impedance layers that prevent redox reactions. Such antibiofouling (a-BF) coatings may also suffer from low durability, repeatability, and scalability, therefore inhibiting POC diagnostics and the commercial development of a biosensing tool from a manufacturing perspective.[19,20] In fact, biofouling remains an important and long-standing challenge in electrochemical biosensing as continuous efforts are still required to enable on-field analyses in biological fluids through commercially viable devices.[12−14] Here, we attempted to meet these demands through a unique strategy that relies on three cooperative factors, namely, the *in situ* generation of a blocking layer, its nanometric thickness, and the gradual increase in the detection area of a scalable, green, and bare electrode. The latter consisted of hydrophobic graphitic carbon

Received: September 28, 2021
Accepted: December 23, 2021
Published: January 6, 2022

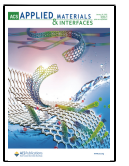

from paper pyrolysis. The nonionic surfactant polysorbate 20, also termed as Tween 20 (T20), generated a hydrophilic 2 nm coating on the electrode that inhibited the biofouling while providing the gradual flow of samples into deeper paper pores, thus leveraging redox reactions across both (i) only partially fouled and (ii) fresh pyrolyzed graphitic paper (PGP) surfaces with increasing detection areas.

Cost-effective, abundant, and sustainable paper has been employed as a raw material for creating pyrolysis-based electrochemical paper-based devices (ePADs).[21,22] Pyrolysis on a furnace delivers a scalable method to fabricate carbon electrodes, which is further free of liquid chemicals and waste generation. Thus, electrodes based on PGP are also an ecofriendly strategy to produce ePADs.[23,24] Pyrolysis converts the entire thickness of cellulose into a conductive and 3D porous graphite-like material due to the formation of sp^2 carbon bonds.[25−29]

During the exposure of the sensor to the samples, T20 resulted in the *in situ* formation of a nanocoating on the top surface and into the porous PGP bulk. This adsorption is irreversible,[30] and it produced herein an interface with a-BF property. The T20 nanocoating further did not notably impair the electron-transfer kinetics and acted as a trigger for the capillarity of aqueous media through the PGP bulk as described above. When drop-casting samples and T20 onto the PGP, these phenomena behaved synergistically to enhance the sensibility that further increased over long-term incubations. While the methods addressed in the literature are generally unable to balance the trade-off among a-BF and sensing performances,[1,2] our approach reached values of sensibility that were even superior to the one achieved in the absence of proteins.

2. EXPERIMENTAL SECTION

2.1. Chemicals. The standard solutions consisted of analytical-grade chemicals dissolved in deionized water (purified in Milli-Q system) at specific concentrations. Potassium ferrocyanide ($[Fe(CN)_6]^{4-}$) and potassium ferricyanide ($[Fe(CN)_6]^{3-}$) were purchased from Merck (Darmstadt, Germany) and Nuclear (Guarulhos, Brazil), respectively. Phosphate buffer saline solution (PBS), potassium chloride (KCl), BSA, T20, fetal bovine serum (FBS), gold(III)chloride trihydrate ($HAuCl_4{\cdot}3H_2O$), and sodium citrate ($Na_3C_6H_5O_7$) were purchased from Sigma-Aldrich (St Louis, MO). The silver ink was provided by SPI (PA, USA).

2.2. Electrode Fabrication. In brief, Whatman #1 filter papers were cut (~2.5 cm × 11 cm) and placed into a tube furnace (Lindberg/Blue M from Thermo Fisher Scientific, NC, USA). First, nitrogen gas (99.99%) was let to flow at 20 L min^{-1} for 5 min before the heating step. Then, the tube was heated from 25 to 1000 °C at 20 °C min^{-1}, kept at 1000 °C in an inert atmosphere for 1 h, and then allowed to cool at room temperature.[27] After pyrolysis, small pieces of pyrolyzed paper were cut and electrically connected to platinum trails patterned on glass slides. Then, polymeric layers of Parafilm M and the adhesive were perforated and positioned onto the PGP for delimiting the detection area. The final step consisted of heating the electrodes at 120 °C for 12 min (Figure S1).

2.3. Electrochemical Analyses. The electrochemical experiments were conducted using the pyrolyzed paper, a platinum wire (1 cm^2), and Ag/AgCl (Metrohm, 3.0 mol L^{-1} KCl) as the working, counter, and reference electrodes, respectively. Cyclic voltammetry (CV) and electrochemical impedance spectroscopy (EIS) assays were performed in an Autolab Metrohm potentiostat (AG PGSTAT302N). The supporting electrolyte was a solution containing PBS (0.1 mmol L^{-1}) and KCl (1.0 mol L^{-1}). The redox probe $[Fe(CN)_6]^{3/4-}$ was added in the supporting electrolyte to monitor Faradaic currents in the presence and absence of T20. Normally used to study the electrode performance, this probe (hydrodynamic radius lower than 1.0 nm)[31] undergoes inner-sphere, reversible, and one-electron redox reactions.[10] In a typical control experiment, the electrodes were exposed to the supporting electrolyte containing the probe, that is, $[Fe(CN)_6]^{3/4-}$ (1.0 mmol L^{-1}), and cyclic voltammograms were registered at 20 mV s^{-1} after different periods of incubation from 5 to 120 min.

To increase the current and create an a-BF nanolayer, we added T20 (0.5% v/v) in the supporting electrolyte containing the redox probe and eventually BSA. The voltammograms were recorded as described above. BSA (isoelectric point: 4.7) is electrically neutral under physiological conditions.[10] This protein was chosen as the biofouling model by accounting for roughly 60% of the total proteins in blood plasma. Thus, BSA (1.0% wt) was added in the supporting electrolyte containing the redox probe to evaluate the electrochemical performance of the method facing an adverse biofouling scenery.

2.4. Characterization. The working electrodes incubated in the presence and absence of T20 were characterized by scanning electron microscopy (SEM, FEI Quanta 650 FEG), energy-dispersive X-ray spectroscopy (EDS, Oxford Instruments), atomic force microscopy (AFM, ParkSystems NX10), contact angle measurement (Attension Theta Lite), laser scanning confocal microscopy (LSCM, Keyence VK-X200), Raman spectroscopy (XploRA Plus Horiba), X-ray photoelectron spectroscopy (XPS, Thermo Scientific), computerized microtomography (μCT, SkyScan1272 Bruker), transmission electron microscopy (TEM), and scanning transmission electron microscopy (STEM, JEOL JEM 2100 FEG-TEM). Topography and capacitance gradient (dC/dZ) measurements were both performed by AFM. Details on the prior characterization experiments are described in the Supporting Information.

2.5. COVID-19 Screening. For engineering the biosensor, we used the recombinant spike (S) protein of the severe acute respiratory syndrome coronavirus 2 (SARS-CoV-2, cultivated in HEK 293 cells and purified by affinity chromatography)[32] as the bioreceptor to recognize the COVID-19 antibodies (Abs). Provided by the Cell Culture Engineering Laboratory of COPPE/UFRJ, this protein was diluted in PBS (concentration of 4.0 mg mL^{-1}, the same utilized in ELISA immunoassays). Patient serum samples were acquired from a cell bank (Biobank, BCRJ, Rio de Janeiro). The incidence of SARS-CoV-2 in the sera was confirmed via Ab detection by the Medtest SARS-CoV-2 IgG/IgM Rapid Test Cassette (Lot COV20030081). Sera from SARS-CoV-2-negative donors were collected before the coronavirus disease 2019 (COVID-19) outbreak (Ethical Appreciation Presentation Certificate approved by the Plataforma Brasil: 43139921.2.0000.5594).

The data attained by the PGP electrodes were compared with the results recorded by a glassy carbon (GC) electrode. The latter was selected by being a well-known carbon electrode for electrochemical analyses. The GC electrodes were polished with 0.3 mm alumina slurries to get mirror-like surfaces. Then, the electrode was washed with water and cleaned in an ultrasonic bath for 15 min.

For performing the immunosensing assays, 6.0 μL of gold nanoparticles (AuNPs) was added on the electrodes and dried for 1 h at room temperature. Then, 6.0 μL of S protein (4.0 mg mL^{-1}) was deposited on the top of the prior electrode surface, dried at room temperature for 30 min, and washed with PBS buffer. Afterward, the electrodes were placed in contact with 6.0 μL of serum samples (diluted 1:250 in PBS) for 30 min, washed for 10 s in PBS, and challenged in EIS analyses for the redox probe. The immunoassays using PGP electrodes and T20 followed the same protocol but with the prior addition of T20 (300.0 μL, 1 h) to provide the flow of the AuNPs and S protein.

The EIS experiments were performed in the electrolyte by applying the half-wave potential ($E_{1/2}$) of the prior cyclic voltammogram (approximately 24 mV) with a frequency range from 0.1 Hz to 30.0 kHz. The data were treated using the NOVA 2.1.3 software. All the analyses were performed at room temperature.

2.6. Gold Nanoparticles. The AuNPs were synthesized according to the simple, low-cost, and stable Turkevich−Frens method.[33] We used $HAuCl_4{\cdot}3H_2O$ (23.0 mg) in deionized water (95.0 mL), which

https://doi.org/10.1021/acsami.1c18778
ACS Appl. Mater. Interfaces 2022, 14, 2522−2533

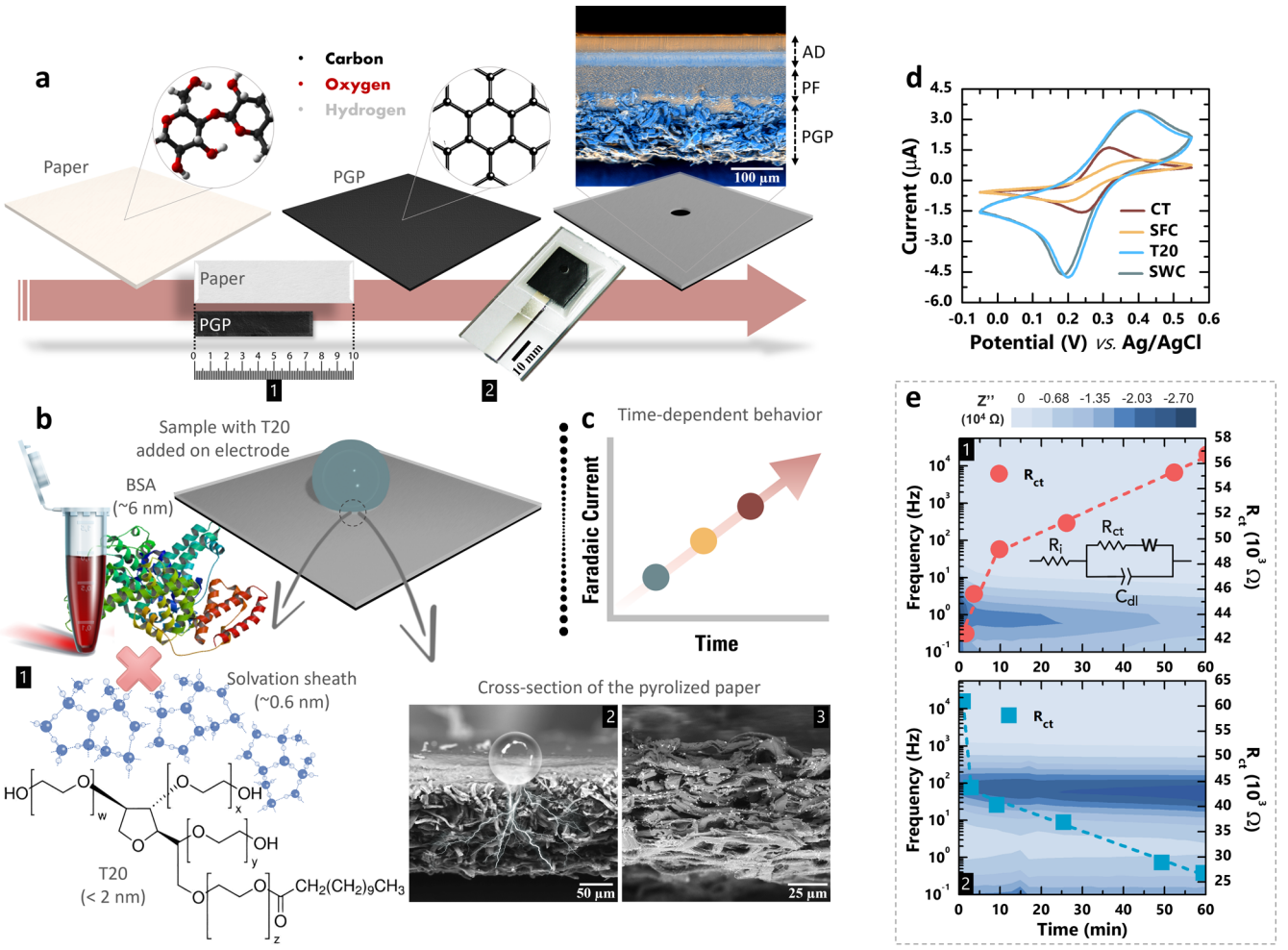

Figure 1. Electrode fabrication, sensing principle, and preliminary electrochemical analyses. (a) Electrode fabrication, chemical structures, and cross-sectional SEM image of adhesive (AD) and Parafilm M (PF) on PGP. Generic representation of the decrease in the area (50%) of paper after pyrolysis (1) and optical image of the electrode (2). (b) Phenomena generated by T20, that is, a-BF ability by forming a solvation sheath (1) and sample flow through PGP pores, as depicted by SEM images of the paper cross section below the detection area (2,3). Illustrations of the T20, solvation layer, and BSA (out of scale) are also displayed in (1) (their dimensions are underlined). The T20-triggered capillarity is generically illustrated in (2). In (3), KCl salts precipitated after electrolyte solvent evaporation can be seen on PGP bulk. (c) Behavior of the resulting Faradaic currents over the course of analyses with T20. (d) Voltammograms of 1.0 mmol L^{-1} $[Fe(CN)_6^{3/4-}]$ (n = 5) under four conditions: control (only the probe), surfactant-free condition (SFC) with BSA, with surfactant only (T20), and surfactant-with condition (SWC) with BSA. Detection was conducted after 5 min of the addition of T20. (e) Color maps of Z'' and R_{ct} over 1 h exposure to probe (n = 3) under the conditions SFC (1) and SWC (2) with BSA. R_{ct} was calculated from the Randles circuit (inset). R_i, C_{dl}, and W mean, respectively, ionic resistance of solution, electric double-layer capacitance, and Warburg element.

was next heated to 100 °C in an Erlenmeyer flask. In parallel, a solution of $Na_3C_6H_5O_7$ (1% w/v) was also heated to 100 °C and then added to the stirred gold medium (5.0 mL). The mixture was stirred until it reached a red color, and then it was allowed to cool naturally. The dispersions were stored at room temperature. To obtain the hydrodynamic diameter and surface charge of the AuNPs in the presence and absence of the S protein, we utilized dynamic light scattering and electrophoretic light scattering, respectively, as detailed in the Supporting Information.

3. RESULTS AND DISCUSSION

3.1. Electrode Fabrication and Sensing Principle. Pyrolyzed strips of chromatography paper were covered by 2 mm perforated sheets of Parafilm M and adhesive to engrave the detection area (Figures 1a and S1). From an image of SEM, the Parafilm M permeated the top of the PGP at a depth of ~16 μm, adding flexibility to this initially fragile electrode. The pyrolysis-induced conversion of cellulose into a conductive graphite-like material is due to the formation of sp^2-hybridized C=C bonds as aforesaid.[25−29] This process was confirmed through analyses by Raman spectroscopy (Figure S2).

T20 promotes the *in situ* formation of an irreversible coating on the PGP surface and bulk due to its amphiphilic nature that originates from three polyethylene oxide (PEO) branches connected with a linear aliphatic chain.[34,35] While these long tails are adsorbed on PGP through hydrophobic interactions, the PEO segments extend into water, behaving as hydrogen-bond acceptors. Thus, these molecules render the PGP surfaces charge-neutral and highly hydrophilic by implying the creation of a strongly solvated environment that the probes can diffuse through while simultaneously preventing hydrophobic and electrostatic interactions with proteins.[36−38] This a-BF ability (Figure 1b) combined with the nanometer thickness (~2 nm) of the T20 coating (it minimizes the blockage of the electron-transfer kinetics) and the T20-triggered sample

https://doi.org/10.1021/acsami.1c18778
ACS Appl. Mater. Interfaces 2022, 14, 2522−2533

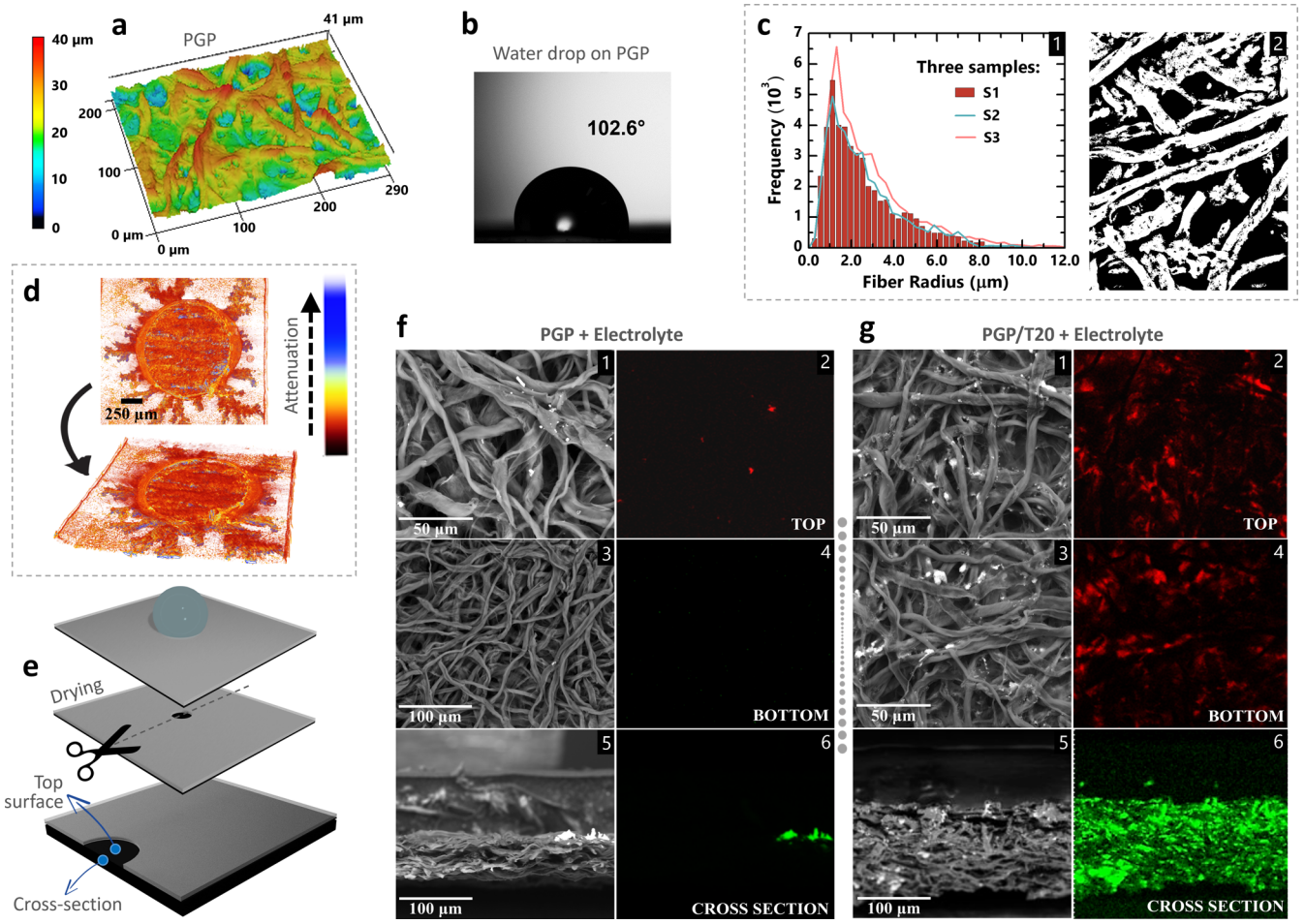

Figure 2. Morphology and topography of PGP and solution capillarity evaluation. (a) 3D LSCM map. (b) Contact angle for a water drop. (c) Histogram distribution of the fiber radius for three different samples (S1−S3). Its inset exhibits a typical SEM image treated to calculate the surface porosity parameters. (d) 2D and 3D μCT images after exposing PGP to T20 with the electrolyte for 1 h, followed by 1 day of drying. (e) Illustrations of the two PGP regions on the sensing zone for SEM and EDS analyses after 1 h of incubation and 1 day of drying, namely, top surface and cross section, as highlighted. SEM images and EDS maps without (f) and with (g) T20 of the top (1,2), bottom (3,4), and cross-sectional (5,6) regions of PGP. The green and red data in EDS maps correspond to 1.0 mol L^{-1} K^+ and Cl^- ions that are found in the electrolyte, respectively.

capillarity through the PGP bulk (it leverages redox reactions across fresh surfaces with increasing electrodic areas) led to the enhancement of the Faradaic currents and sensibility, which further increased over long-term exposures in biological fluids (Figure 1c).

3.2. Preliminary Electrochemical Analyses. The electrode performance was first studied via CV, with the working electrodes being cycled between the oxidation and reduction of 1.0 mmol L^{-1} $[Fe(CN)_6]^{3/4-}$ (n = 5) under different conditions (Figure 1d). All the systems displayed transient voltammograms that reflect a semi-infinite linear diffusion profile, as verified in the macroelectrodes.[8,39] PGP and PGP/T20 led to quasi-reversible redox processes with high heterogeneous electron-transfer rate constants (Figure S3 and Table S1).[40] Notwithstanding the T20 coating-induced increase in average peak-to-peak separation (ΔE_p) from 90 to 193 mV, the peak currents increased by a factor of 3 over the original values (Figure S4). This signal amplification can be ascribed to the nanocoating-triggered capillarity by allowing for the redox probe to access increasing electrode areas. Conversely, as expected, BSA impacted the currents and ΔE_p was found to be 268 mV due to the PGP biofouling. When challenging the PGP/T20 system in the BSA solution, nonetheless, the electrochemical performance was similar to that noted when adding only T20 (without BSA), thus suggesting the a-BF and signal amplification features of this coating. One should also stress that both systems, without and with T20, showed diffusion-controlled mass transport (Figure S3), and their quasi-reversible nature is likely due to the carbon surface properties (functional groups, e.g., C−O, C═O, and O═C−O and surface roughness, Figure S5) and low resistivity of the PGP (128 mΩ cm).

The gradual penetration of the probe solution through the PGP pores with resultant hindrance-free redox reactions across increasing fresh (no fouled) electroactive areas also caused a decrease in the charge-transfer resistance (R_{ct}) and imaginary impedance (Z'') according to analyses by EIS over exposures to T20 and BSA for 1 h (n = 3, Figure 1e). These changes were especially high until 3 min, meaning that the capillarity kinetics is primarily high over the first few minutes of incubation. Otherwise, Z'' and R_{ct} increased with no T20 being used, as expected.

3.3. Electrode Features and Capillarity through Paper. Chemically, the PGP surface was especially composed of C═C sp^2 (53.4%) and C−C sp^3 (14.3%) according to the XPS data (Figure S5). From the analyses of LSCM and contact

https://doi.org/10.1021/acsami.1c18778
ACS Appl. Mater. Interfaces 2022, 14, 2522−2533

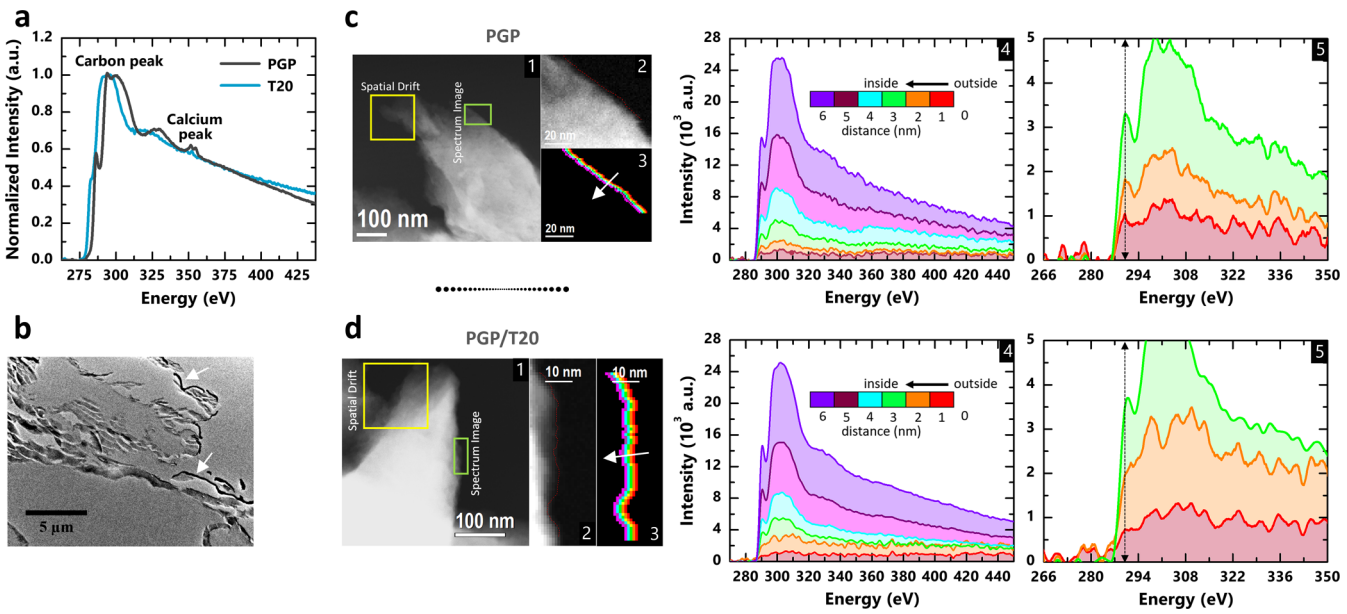

Figure 3. Nanoscale thickness of the T20 coating. (a) EELS spectra of PGP and T20. (b) TEM image of a slice of PGP prepared by ultramicrotomy. Thin layers of Au (deposited to identify the PGP top surface) correspond to the darkest contrasts, being indicated by white arrows. STEM images and EELS spectra of (c) PGP only and, (d) PGP exposed to T20. STEM images (1) along with amplified regions (2) as indicted by the green highlights in (1). Colored lines in these amplified regions indicate the areas used to integrate the EELS signals from the outside into the samples as indicated by the arrows (3). Each line means 1 nm. Resulting EELS integrated spectra in association with the colored lines as discriminated (4) and zoom of the first three spectra, with arrows highlighting the π peaks at around 287 eV (5).

angle (θ), PGP presented rough (5.7 ± 0.9 μm in root-mean-square roughness) and hydrophobic (102.6° in θ) surfaces as expected (Figures 2a,b and S6). Further, three PGP samples had similar fiber and pore distributions (Figures 2c and S7). The mean diameters of the fibers and pores were 4.0 ± 0.3 and 11.9 ± 1.0 μm, respectively (Table S2). These low deviations agree with the good reproducibility that was achieved throughout this work for hundreds of tested PGPs (more than 450).

After the exposure of PGP to T20 in water, θ dropped down to zero in less than 2 s (Video S1) due to liquid capillarity. The same result was verified after addition of water on a previously treated PGP as follows: 1 h incubation in T20, washing, and 1 day drying (Video S2). This capillarity even after the washing and drying of the electrodes indicates the irreversible adsorption of the T20 coating.

The liquid capillarity after 1 h exposure of PGP to T20 was evaluated by μCT, SEM, and EDS. The electrolyte in the absence of T20 kept itself only on the top of PGP, whereas T20 with exposures enabled the radial and heterogeneous advancement of the electrolyte (Figures 2d and S8) through the entire PGP bulk even beyond the top detection area (Figures 2e–g and S9–S12). This liquid capillarity reached distances beyond the sensing area of up to 2.3 mm.

3.4. Adsorption and a-BF Ability of T20. Having confirmed the radial penetration of the solution through the pores of the PGP/T20 system, we turned our attention to prove the presence of the T20 layer on PGP and to assess its nanometer scale and a-BF property. The occurrence of this polysorbate on the surface of PGP was confirmed through XPS measurements by considering (i) the decrease in the C sp^2/sp^3 ratio (3.74 for PGP and 0.08 for PGP/T20 after 1 h exposure and washing) and (ii) the increase in the relative quantity of oxygen (ratio between O 1s and C 1s peaks of 0.03 for PGP and 0.24 for PGP/T20, Figure S5). The nanometric thickness of the T20 coating was first confirmed onto smooth surfaces, that is, mica and silica, by AFM (Figure S13). The thicknesses were 2.8 ± 0.2 nm (mica, n = 6) and 2.1 ± 0.3 nm (silica, n = 3). A value of roughly 2 nm was also indicated by TEM onto rough PGP as discussed next. This reduced thickness is key to not significantly impair the electron-transfer kinetics, thus working synergically with the sample capillarity and T20 a-BF property for assuring application in complex biological fluids.

PGP, T20, and BSA could be identified through their electron energy loss spectroscopy (EELS) spectra (Figure 3a). The nitrogen (N) peaks, for instance, indicated the occurrence of BSA (Figure S14). As shown in the TEM images of ultramicrometric slices of PGP (Figures 3b and S15), the PGP fibers had diameters of roughly 200 nm. The images by STEM and EELS spectra were obtained for bare PGP and after 1 h incubation in T20 (Figure 3c,d). The EELS responses were integrated through lines corresponding to a thickness of 1 nm. These lines extended from where the first signal was identified inward toward the samples. In almost all spectra, we observed two well-defined peaks that are ascribed to p (~287 eV) and s (~304 eV) peaks of bare PGP. In contrast, the first two spectra for the PGP/T20 system revealed the incidence of a shoulder in the p peaks that was the signature of T20. This data suggests the formation of a coating consisting of this polysorbate with a 2 nm thickness on the PGP, which implies the adsorption of a T20 monolayer, in agreement with the values achieved onto the smooth surfaces of polystyrene (2.1 nm)[30] and octadecyltriethoxysilane (1.9 nm).[41]

The a-BF property of the T20 nanocoating was first studied by XPS and electrical tests from AFM. The attribute of T20 in protecting the electrode surface from BSA-induced biofouling was first revealed by XPS (Figure S5). While the N/C ratio (peaks 1s) was obtained as 0.10 for PGP/BSA, this parameter was reduced to 0.04 for the system PGP/T20/BSA, therefore showing a decrease in the relative quantity of adsorbed BSA

https://doi.org/10.1021/acsami.1c18778
ACS Appl. Mater. Interfaces 2022, 14, 2522–2533

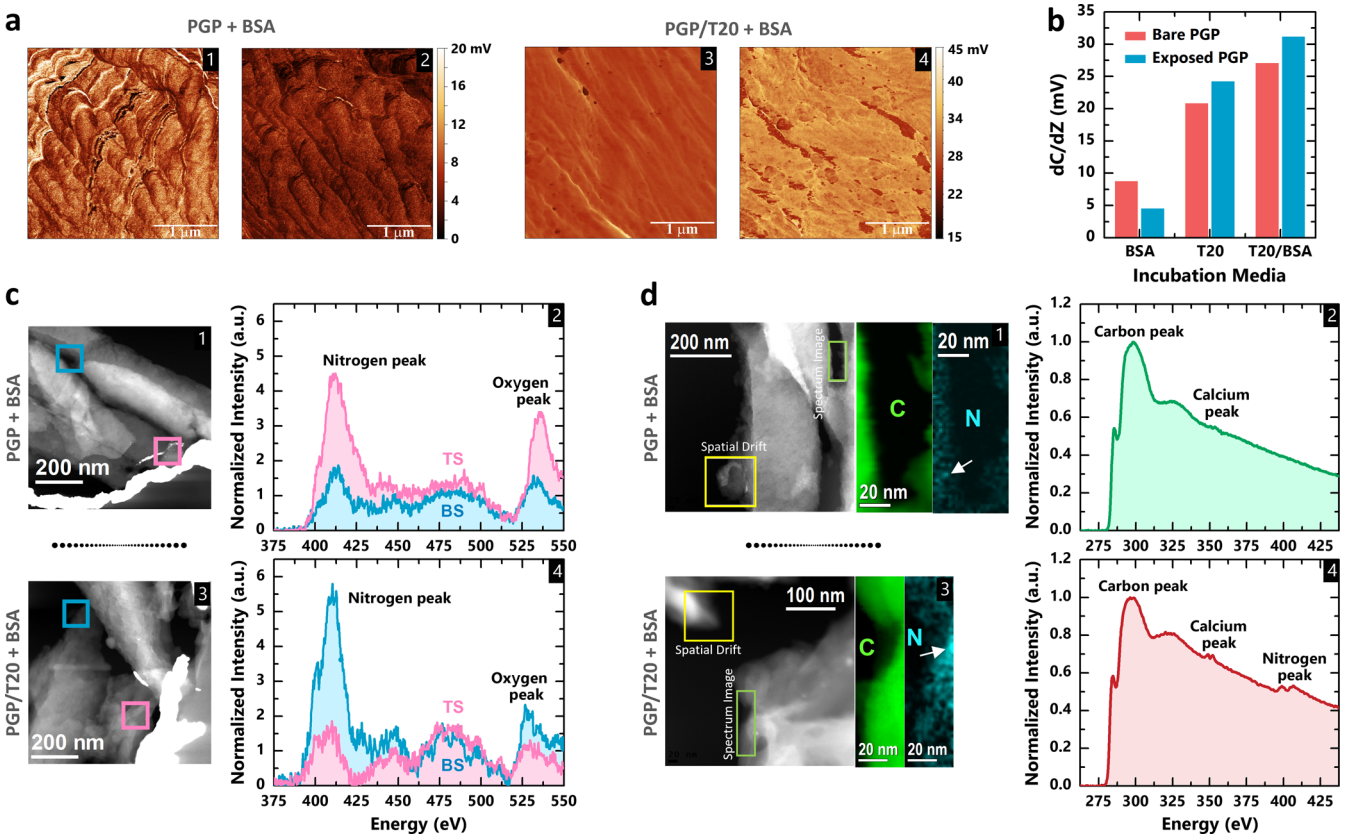

Figure 4. a-BF ability of the T20 nanocoating. (a) dC/dZ maps of PGP. (b) Values of dC/dZ of PGP after exposure to distinct solutions as indicated. In (a,b), the same area (9 μm^2) was analyzed for each case before and after the steps of incubation. (c) STEM images and EELS spectra of PGP surfaces. The gold layer is the lightest contrast in these images. Pink and blue boxes in the STEM images indicate the regions where the EELS spectra were attained, that is, few and hundreds of nanometers bellow the Au layer that were called as the top surface (TS) and bottom surface (BS), respectively. Each spectrum corresponds to an average of eight spectra collected from such marked regions. (d) STEM images, maps of C and N, and EELS spectra of PGP surfaces. These analyses were proceeded microns away from the Au top layer. The EELS spectra were extracted in the regions with maximum intensities in the N maps, as highlighted by white arrows. In a, c, and d, we made analyses using PGP after exposures to BSA only (1,2) and subsequent exposures to T20 and BSA (3,4).

(indicated by the nitrogen peak) when previously adding T20 on the paper. Concerning the electrical tests from AFM, these analyses were aimed to attain the dC/dZ. These values express the capability of an area of undergoing electrical polarization.[42] The biofouling of PGP by BSA impaired dC/dZ by 46.7% after 1 h of exposure. With only T20 being added (1 h), conversely, dC/dZ increased by 16.1% that is likely due to the oxygen groups present in this species (Figure S16). Impressively, the dC/dZ for the PGP/T20/BSA system was similar to the one for PGP/T20 (Figures 4a,b), thereby indicating the biofouling-resilient characteristic of T20 as well. Such a feature was further confirmed via TEM.

In the STEM images and EELS spectra (achieved after 1 h of exposure to BSA and following 1 h of exposure to T20 and BSA, Figure 4c), while BSA was monitored only on the PGP top in the absence of T20, as expected, the N peak in this region was comparable with the background signal when probing the PGP/T20 system. This finding shows the ability of T20 to inhibit the BSA adsorption, that is, its a-BF ability. Conversely, this protein was detected on hundreds of nano- and micrometers below the PGP/T20 top (Figures 4d and S17). This outcome is likely because of the inability of the washing routine (after each incubation) to remove the BSA solution from the bulk of PGP. Hence, we hypothesized that this protein is not originally adsorbed on the PGP, but it originates from the solvent evaporation.

3.5. Time-Dependent Sensing Performance. In order to properly investigate the electrochemical performance of our system, further measurements were made over 1 h exposures. Cyclic voltammograms disclosed a linear increase in the anodic (I_{ap}) and cathodic (I_{cp}) peak currents (Figure 5a,b) when detecting 1.0 mmol L^{-1} $[Fe(CN)_6]^{3/4-}$ in the presence of T20 and BSA. The rate of this increase for I_{cp} was ~22-fold higher than the one obtained by the PGP with no T20 added, whose performance was significantly impaired by biofouling (Figure 5c). Further CV analyses were performed by changing the probe concentration (1.0 to 5.0 mmol L^{-1}) for sensibility evaluation. The sensibilities ranged from 1.7 (5) to 3.5 μA mmol L^{-1} (60 min exposure) for I_{ap} (Figures 5d,e and S18 and S19). The latter is even higher than the ones reached by a traditional gold disk electrode (1.4 μA mmol L^{-1}, Figure S20) and PGP (2.4 μA mmol L^{-1}) without T20 and BSA (control condition). As expected, the performance of the T20-free PGP electrode was deteriorated by the BSA biofouling.

Three PGPs for each one of the probe concentrations (n = 5 for each electrode) were used in the previous analyses. The low confidence intervals (n = 15) as attained (Figures 5b,d and S18) indicate good reproducibility. While this one-step procedure is ideal for on-field measurements by reducing the

https://doi.org/10.1021/acsami.1c18778
ACS Appl. Mater. Interfaces 2022, 14, 2522−2533

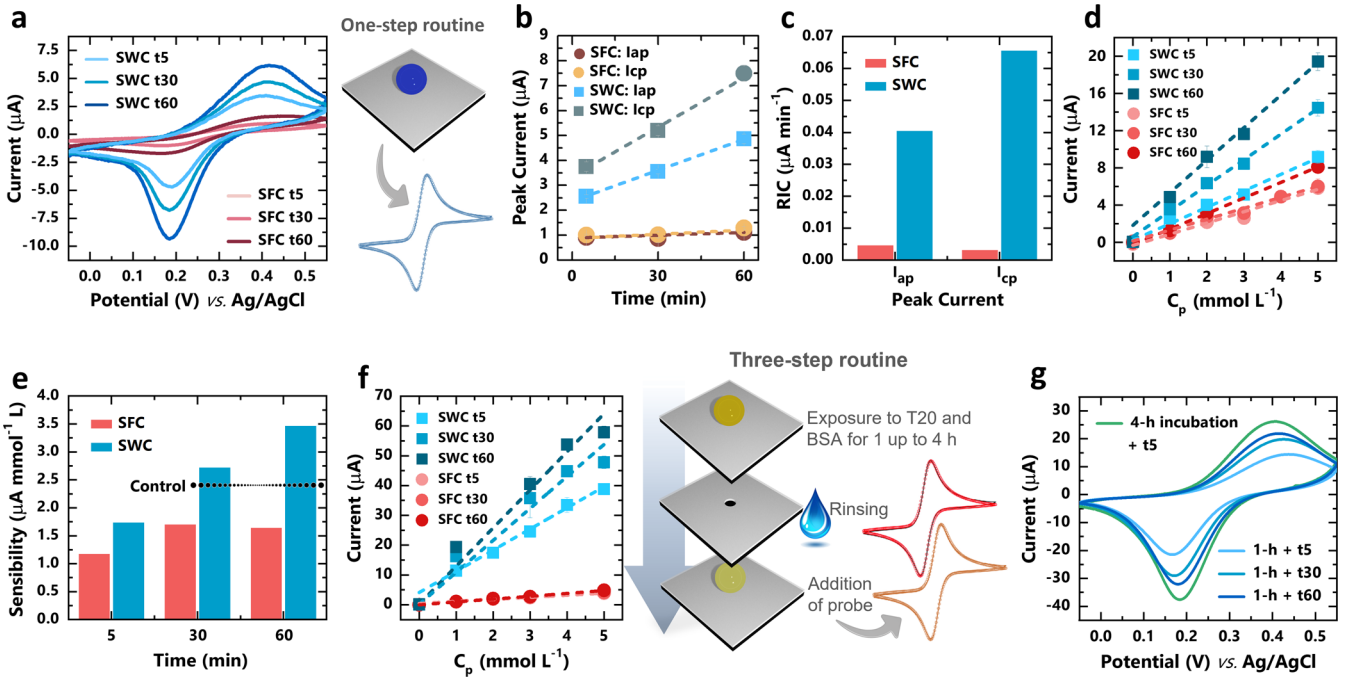

Figure 5. a-BF and electrochemical performances. (a) Voltammograms of 1.0 mmol L^{-1} $[Fe(CN)_6]^{3/4-}$ under the surfactant-free (SFC) and surfactant-with (SWC) conditions after 5 (t5), 30 (t30), and 60 min (t60) of exposure to BSA. (b) Resulting peak currents and, (c) rate of increase in these currents (RIC) as stressed. (d) Analytical curves for probe standards under SFC and SWC conditions over t5, t30, and t60. (e) Resulting sensibilities for I_{ap}. The dotted line means that the sensibility reached under the control condition, that is, without T20 and BSA. The prior analyses (n = 15) were based on the one-step routine as illustrated in the inset of a, with simultaneous exposure to probe, BSA, and T20 (when used). (f) Analytical curves for probe standards under the SFC and SWC conditions using the three-step routine, as illustrated herein with 1 h incubation in BSA without and with T20. The detection was performed after t5, t30, and t60 of the addition of $[Fe(CN)_6]^{3/4-}$ (n = 5). (g) Voltammograms from this three-step routine after 1 and 4 h incubations in BSA with T20 (n = 5).

user error risks,[2] a common practice in bioanalyses involves the steps of incubation in the sample, rinsing, and exposure to the solution for electrochemical sensing.[2,3] In this regard, the PGP performance was also scrutinized facing this three-step procedure. The BSA solution with or without T20 was added on the electrode for 1 h, followed by rinsing, addition of the probe (1.0−5.0 mmol L^{-1}), and detection after 5, 30, and 60 min.

The T20 nanocoating is expected to remain after rising due to its irreversible adsorption,[30] enabling the probe capillarity through PGP and ultimately increasing the sensibility as it was indeed noted herein (Figure S21). High sensibilities were reached by the PGP/T20/BSA system, for example, 17.7 μA mmol L^{-1} for I_{ap} at 60 min(n = 5, Figures 5f and S22). The sensibilities by the PGP/BSA system remained similar over the experiments (1.0 μA mmol L^{-1}). Exposures to T20 and BSA were also performed for 4 h (Figure 5g). The currents after 5 min of the addition of the redox probe were 19.6% (I_{ap}) and 17.1% (I_{cp}) higher than the data at 1 h exposure, signaling the potential of the method toward long-term experiments.

T20 with PGP enabled a relevant gain in sensibility through a tunable and simple way, dispensing strategies such as the modification with nanomaterials (via direct adsorption, layer-by-layer entrapment, or covalent cross-linking).[23] This increase in the sensing performance can be ascribed to three cooperative factors: the a-BF property of T20, its nanometric thickness, and the solution capillarity through PGP pores as the probe is allowed to undergo redox reactions across only partially fouled surfaces and also across fresh surfaces with increasing detection areas. From the analyses of double-layer capacitance (Figure S23),[43] the electroactive area of the T20-free PGP (0.4 10^{-3} cm^2) increased to 23.1 10^{-3} and 26.9 10^{-3} cm^2 after incubation in the probe solution with T20 for 30 and 60 min, respectively. In this way, remarkably, the electroactive area upon adding T20 onto PGP was up to 67-fold higher than the area in the absence of this surfactant.

3.6. Proof-of-Concept Application: Unprocessed Samples. To attain a comprehensive understanding on the method performance in unprocessed and real-world biological samples, we first challenged the electrodes in undiluted human plasma and FBS. Using the three-step protocol with 1 h T20-free exposure to plasma (Figure S24), practically no Faradaic current to 1.0 mmol L^{-1} $[Fe(CN)_6]^{3/4-}$ (n = 5) was detected. Otherwise, the PGP/T20 system could enable high peak currents that once again increased over time. The I_{ap} data were 2.9 (5), 3.2 (30), and 3.6 mA (60 min) that are similar to the values from the one-step assay in the presence of BSA only. The I_{ap} at 60 min was 5.8 times higher than the original current (under the control condition).

The electrodes were further challenged in plasma and FBS with the prior addition of T20 (1 h) followed by the three-step protocol as described above, with the addition of the sample, washing electrolyte, and probe (n = 3). Compared with the simultaneous addition of T20 and plasma, the increase in peak currents over time was found to be more prominent when allowing for the adsorption of T20 on PGP before adding the sample (Figure 6a,b). In this case, the I_{ap} at 60 min increased by a factor of 12.5 over the original peak currents. Similar results were noted for the analysis of unprocessed FBS (Figures 6b and S25).

In terms of the a-BF feature, while the undiluted samples impacted the charge-transfer kinetics (ΔE_p > 500 mV), as

https://doi.org/10.1021/acsami.1c18778
ACS Appl. Mater. Interfaces 2022, 14, 2522−2533

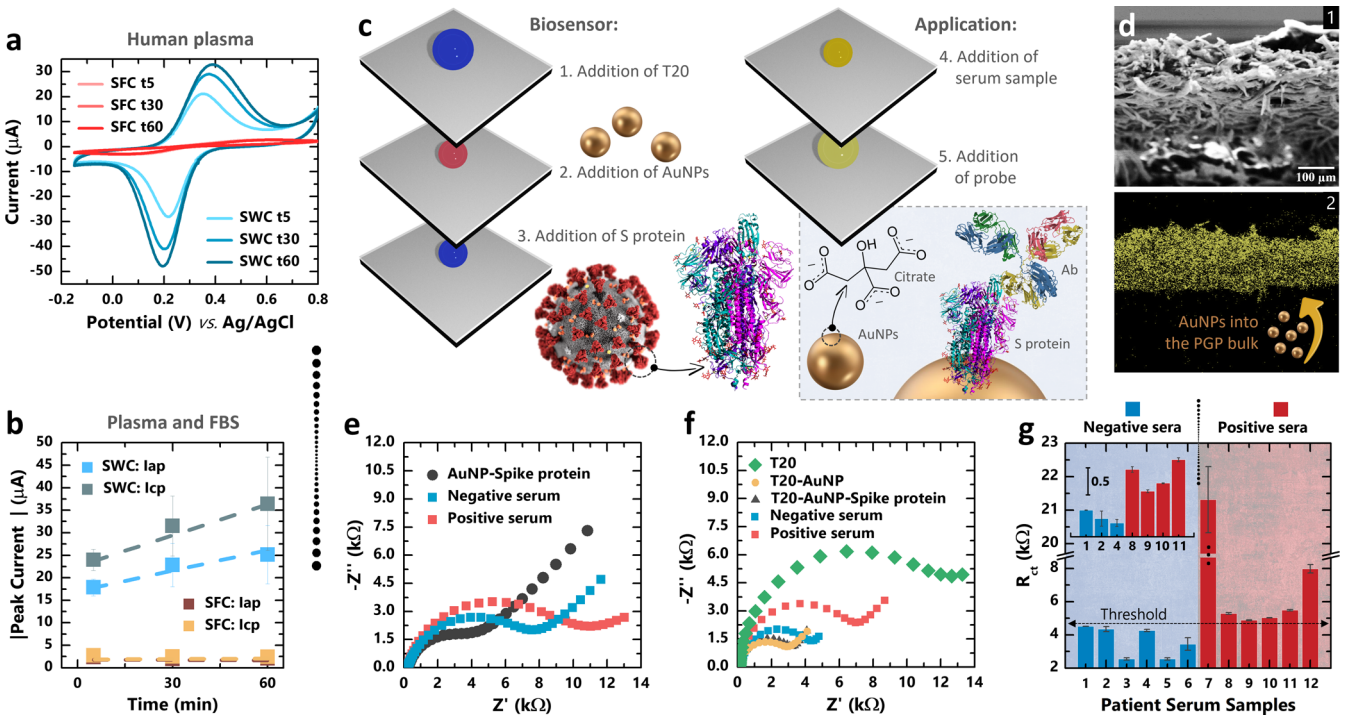

Figure 6. Proof-of-concept applications to human plasma, FBS, and patient sera for COVID-19 screening. (a) Voltammograms of 1.0 mmol L^{-1} $[Fe(CN)_6]^{3/4-}$ under the SFC and surfactant-with SWC conditions with prior addition of T20 followed by the three-step procedure with 1 h incubation in plasma. The detection was conducted after 5 (t5), 30 (t30), and 60 min(t60) of the addition of the probe. (b) Resulting peak currents from this type of investigation considering the global average data for plasma and FBS. (c) Steps of the immunoassays for sensing COVID-19 Ab and illustrations of the negatively charged citrate-adsorbed AuNPs, the direct adsorption of the S protein on these nanoparticles, and the protein-Ab binding. (d) SEM image (1) and EDS map (2) of the PGP cross section with T20 used. The yellow data in EDS map relates to AuNPs, as indicated by the arrow. (e) Nyquist plots of 1.0 mmol L^{-1} $[Fe(CN)_6]^{3/4-}$ by GC electrodes for the systems AuNP−S protein, AuNP−S protein-negative serum, and AuNP−S protein-positive serum using the three-step routine without T20. Z' means the real impedance. (f) Nyquist plots of 1.0 mmol L^{-1} $[Fe(CN)_6]^{3/4-}$ by PGP from first scans for T20, T20-AuNPs, T20-AuNPs-S protein, T20-AuNPs-S protein-negative serum, and T20-AuNPs-S protein-positive serum. (g) Average R_{ct} from first scans utilizing two independent electrodes for each sample, that is, sera taken from healthy (1−6) and COVID-19 patients (7−12). Its inset displays the R_{ct} (scale bar in kΩ) related to some samples for underlining their discrepancies.

expected, both the procedures based on the simultaneous addition of T20 and the sample and the prior addition of T20 were capable of protecting PGP from the nonspecific binding of proteins, affording quasi-reversible redox processes. The first case led to ΔE_p of 127 ± 3 mV (plasma), whereas the second one resulted in ΔE_p values of 160 ± 8 mV (FBS) and 170 ± 33 mV (plasma, Table S3). These values are lower than the ΔE_p obtained by the one-step protocol (roughly 200 mV; see Figures 1d and 5a,g). This result is likely due to the partial removal of proteins poorly adsorbed on PGP by the washing step before electrochemical detection when using the three-step routine. One should also highlight that such a high protein resistance imparted by the T20 can be attributed to two characteristics of this polysorbate, that is, the presence of multiple PEO chains per molecule and a largely linear hydrophobic chain. These properties are expected to provide the formation of a densely packed and irreversibly adsorbed nanolayer for an effective a-BF property.[36,37]

3.7. Proof-of-Concept Application: COVID-19 Screening. The clinical applicability of the method was investigated in the COVID-19 screening of patient sera by sensing SARS-CoV-2 Abs. COVID-19 pandemic has shed light on the deployment of scalable and field-deployable testing platforms.[1,44,45] The serological tests to detect SARS-CoV-2 Ab carry advantages over nucleic acid and antigen assays that include a much longer detection window (2 up to 3 months) and higher stability of Ab when compared with viral ribonucleic acid (RNA).[46] Further, these tests do not need lab with biosafety level 2 (BSL-2).[47] These features contribute for improving the diagnostic accuracy and translating the approach into the real-world toward mass screening by considering the steps of sample collection, preparation, transport, and storage along with the sensing procedure.[48] While Ab assays struggle to assure early diagnostics due to the lag in the production of Ab, they play a significant role not only in enabling POC assays but also in diagnosing past COVID-19 infection, testing immunity, identifying convalescent plasma donors, and assisting the development of vaccines and therapeutic Abs.[47]

Label-free EIS-based biosensors with direct adsorption (noncovalent functionalization) of the recognizing element (bioreceptor) are particularly prone to nonspecific binding, drifts in the signal (induced by the electrolyte and probe), and even coating leaching in environmentally harsh media such as biofluids.[49−51] Nonetheless, these systems provide crucial features toward daily diagnostics such as fast analyses, the absence of stability issues related to enzymatic labels as used in sandwich biosensors,[23] and a modular architecture as it can be easily tailored to monitor other targets from the simple drop casting of their bioreceptors onto a transducer. Besides, direct adsorption avoids the rehybridization from sp^2 to sp^3 carbon, as verified in covalent functionalization. This phenomenon

https://doi.org/10.1021/acsami.1c18778
ACS Appl. Mater. Interfaces 2022, 14, 2522−2533

diminishes the electronic delocalization and then increases the material resistivity with the sensitivity being damaged.[50] Considering these advantages, we here adapted the method to produce a label-free impedimetric biosensor with the direct adsorption of S protein on AuNPs for sensing SARS-CoV-2 Ab in COVID-19 patient sera (enriched in immunoglobulins G, IgG, and M, IgM). The method relied on simple drop-casting steps (Figure 6c).

To improve sensibility, T20 was added (1 h) to provide the capillarity of the successively added AuNPs (1 h) and S protein (30 min) into the PGP bulk (Figures 6d and S26). The AuNPs favored the transfer of electronic charges across PGP (decrease in R_{ct}) and enabled the noncovalent anchoring of the S protein via electrostatic interactions by presenting negatively charged citrate-adsorbed surfaces (citrate was used as a biocompatible reducer to synthetize AuNPs).[48] The zeta potential and hydrodynamic diameter of the nanoparticles were found to be roughly −29 mV and 34 nm, respectively. This diameter of the AuNP−S protein conjugates increased to 40 nm. While the adsorption of S protein on the AuNPs lasted only 30 min (see Figure 6c), covalent functionalization from the carbodiimide linking chemistry, for example, could be as long as 16 h.[52] Electrostatic interactions are supposed to yield dense and oriented S protein monolayers (10 nm)[53,54] around the nanoparticles. In continuation, the steps of incubation in serum (6 μL, 30 min), washing, and addition of (1.0 mmol L^{-1} $[Fe(CN)_6]^{3/4-}$) onto the PGP for EIS sensing were proceeded. The increase in R_{ct} (from Nyquist plots) with target binding was used as the transducer signal for detecting SARS-CoV-2 Ab.

Compared with the data reached for a healthy individual serum, the increments in R_{ct} for a COVID-19 patient serum increased with the sample dilution, being 11.4, 20.1, and 69.2% for 1:1, 1:5, and 1:250 v/v serum in the electrolyte, respectively. Such a result was expected for this type of immunosensor, as discussed above (Figure S27). Since we believe that the gains gleaned from the use of this platform as aforesaid overperform the requirement of diluting the samples in terms of significance to assure daily diagnostics, the succeeding experiments were made using the highest dilution that rendered reproducible tests with low sample consumption (24 nL per analysis). Despite this high dilution, analyses of the negative serum with GC (same protocol as that used for T20-free PGP) still suffered from biofouling, implying a high R_{ct} (~11 kΩ) that was 56.5% higher than the resistance reached when making the detection without any prior exposure to the serum (Figure 6e). Additionally, nonreproducible data were attained by the PGP in the absence of T20. Nonspecific binding is likely the cause of the nonsystematic drifts in response that were observed in this case.

In contrast, a high clinical accuracy was achieved when using T20. Nyquist plots were obtained from the first EIS scans for each case (n = 10) utilizing two independent PGP electrodes (Figures 6f and S28). The plots displayed semicircle areas and straight lines that mean, respectively, charge-transfer- and diffusion-limited steps.[51] The R_{ct} data showed average deviations from 1.2 up to 155.5 Ω only. In comparison with PGP/T20, R_{ct} reduced from 12.3 to 3.8 kΩ after adding the nanoparticles. This decrease reveals that a high charge-transfer kinetics can proceed across the T20 nanocoating, as expected. Next, the R_{ct} after addition of the S protein (4.4 kΩ) was similar to that resistance for the PGP/T20/AuNP system. Following, the R_{ct} recorded when probing the negative serum (4.5 kΩ) was only 4.6% larger than the one for the PGP/T20/AuNP/S protein system, hence supporting the a-BF ability of T20 in this fashioned immunosensing assay.

PGP/T20 also performed better than GC with regard to the sensibility. Exposures to a positive serum led to an increase in R_{ct} of 53.8 and 69.2% over the results for the negative serum using GC and PGP, respectively. We next expanded this application to 12 sera collected from healthy individuals (6) and COVID-19 patients (6). These samples could be clearly distinguished from each other with 100% accuracy (Figure 6g). Compared with the negative sera, the lowest relative increase in R_{ct} when analyzing a positive serum was 12.1%, whereas the average increase was found to be 130.6%. These data imply that the approach may be adapted to develop label-free and modular immunosensors toward screening applications despite the inability of the washing step in promoting an exhaustive removal of the proteins barely adsorbed into the PGP bulk, as discussed above (Figure 4).

4. CONCLUSIONS

In summary, we have demonstrated that a simple drop-casting method in combination with cost-effective and scalable 3D pyrolyzed paper as the electrode can be utilized to enable sensitive electrochemical tests in complex biofluids. The hydrophilic layer formed by an off-the-shelf polysorbate, T20, inhibits biofouling while allowing for aqueous media accessing the deeper pores of PGP to undergo hindrance-free redox reactions across increasing sensing areas. The nanometric thickness of this protective layer is also crucial by not meaningly impairing the electron-transfer kinetics. While the a-BF layers addressed in the literature usually compromise the sensibility, this method is able to provide both high a-BF and detection performances. The sensibility further increases over long-term incubations.

The sensing platform is promising toward commercial translation by taking up its low-cost and mass-production compatibility. A single device is estimated to cost roughly $0.23 (not considering the bioreceptor for immunosensing assays). With regard to scalability, approximately 20 paper strips can be simultaneously pyrolyzed into a conventional laboratory furnace, implying the fabrication of more than 140 PGP electrodes. In addition, 30 standalone structures of PGP can be patterned in a single cutting run using knife plotters.[27] It is also worthwhile to note that the device cost and fabrication time could be further decreased in a large-scale scenery.

The T20 nanocoating can be produced in an *in situ* way or before the addition of the sample, adding flexibility to the approach that outperformed state-of-the-art a-BF coatings in terms of commercial development compatibility as well (Table S4). We believe that this platform may be a valuable solution toward POC and mass screening. In this way, label-free assays with a modular architecture as demonstrated here are attractive by being more easily extended to other targets. However, although the results above for screening of COVID-19 are an encouraging indicator, applications to large-scale patient samples need to be conducted further to reliably scrutinize (i) the rates for false negatives and positives and (ii) the capacity of the biosensor of leveraging the quantification of COVID-19 Ab in comparison with gold-standard techniques. Future efforts should also be devoted to evaluate the immunosensor selectivity and its ability to provide accurate diagnostics of unprocessed sera using, for example, covalent

https://doi.org/10.1021/acsami.1c18778
ACS Appl. Mater. Interfaces 2022, 14, 2522−2533

functionalization of the bioreceptor. In this regard, one should stress that carbodiimidazole-activated T20 adsorbed on carbon surfaces can covalently attach the $-NH_2$ groups of bioreceptors toward immunoassays.[36,37] In addition, while the electrical neutrality of the T20 coating prevented here electrostatic repulsions with $[Fe(CN)_6]^{3/4-}$, charged coatings could also be investigated for the sensing of different probes.

■ ASSOCIATED CONTENT

Supporting Information

The Supporting Information is available free of charge at https://pubs.acs.org/doi/10.1021/acsami.1c18778.

Additional experimental details, mechanical stability and assembly of the electrode, structural evaluation of the pyrolyzed paper, electrochemical performance, chemical composition analysis, and results as highlighted throughout the article, including a comparison of the performance of the approach described herein with strategies published in the literature (PDF)

Spreading of T20 with water drop (10 μL) through porous PGP (MP4)

Spreading of the water drop (10 μL) through porous PGP that was previously treated as follows: 1 h of incubation in T20, washing with water, and 1 day of drying (MP4)

■ AUTHOR INFORMATION

Corresponding Authors

Murilo Santhiago − *Brazilian Nanotechnology National Laboratory, Brazilian Center for Research in Energy and Materials, Campinas, São Paulo 13083-100, Brazil; Center for Natural and Human Sciences, Federal University of ABC, Santo André, São Paulo 09210-580, Brazil;* orcid.org/0000-0002-9146-9677; Email: murilo.santhiago@lnnano.cnpem.br

Renato S. Lima − *Brazilian Nanotechnology National Laboratory, Brazilian Center for Research in Energy and Materials, Campinas, São Paulo 13083-100, Brazil; Institute of Chemistry, University of Campinas, Campinas, São Paulo 13083-970, Brazil; Center for Natural and Human Sciences, Federal University of ABC, Santo André, São Paulo 09210-580, Brazil; São Carlos Institute of Chemistry, University of São Paulo, São Carlos, São Paulo 13566-590, Brazil;* orcid.org/0000-0001-8450-1475; Email: renato.lima@lnnano.cnpem.br

Authors

Caroline Y. N. Nicoliche − *Brazilian Nanotechnology National Laboratory, Brazilian Center for Research in Energy and Materials, Campinas, São Paulo 13083-100, Brazil; Institute of Chemistry, University of Campinas, Campinas, São Paulo 13083-970, Brazil*

Aline M. Pascon − *Brazilian Nanotechnology National Laboratory, Brazilian Center for Research in Energy and Materials, Campinas, São Paulo 13083-100, Brazil; Center for Natural and Human Sciences, Federal University of ABC, Santo André, São Paulo 09210-580, Brazil*

Ítalo R. S. Bezerra − *Brazilian Nanotechnology National Laboratory, Brazilian Center for Research in Energy and Materials, Campinas, São Paulo 13083-100, Brazil; Center for Natural and Human Sciences, Federal University of ABC, Santo André, São Paulo 09210-580, Brazil*

Ana C. H. de Castro − *Center for Natural and Human Sciences, Federal University of ABC, Santo André, São Paulo 09210-580, Brazil*

Gabriel R. Martos − *Brazilian Nanotechnology National Laboratory, Brazilian Center for Research in Energy and Materials, Campinas, São Paulo 13083-100, Brazil; Faculty of Chemistry, Pontifical Catholic University of Campinas, Campinas, São Paulo 13087-571, Brazil*

Jefferson Bettini − *Brazilian Nanotechnology National Laboratory, Brazilian Center for Research in Energy and Materials, Campinas, São Paulo 13083-100, Brazil*

Wendel A. Alves − *Center for Natural and Human Sciences, Federal University of ABC, Santo André, São Paulo 09210-580, Brazil;* orcid.org/0000-0002-8394-2751

Complete contact information is available at: https://pubs.acs.org/10.1021/acsami.1c18778

Author Contributions

R.S.L. and M.S. conceived the sensing strategy and designed the study. C.Y.N.N., I.R.S.B., A.C.H.C., and G.R.M. performed the electrochemical experiments. J.B. conducted the TEM analyses. The other surface characterization investigations were accomplished by A.M.P. with the help of C.Y.N.N. and I.R.S.B., whereas W.A.A. conceived the experimental design of the label-free immunoassay. C.Y.N.N., A.M.P., A.C.H.C., G.R.M., and J.B. treated the data resulting from experiments. R.S.L. and M.S. wrote the paper with the help of C.Y.N.N., A.M.P., I.R.S.B., A.C.H.C., and J.B. All authors discussed the results.

Notes

The authors declare the following competing financial interest(s): The authors Renato S. Lima and Murilo Santhiago are listed as inventors on a patent filing application describing this technology.

■ ACKNOWLEDGMENTS

We would like to thank Maria H. O. Piazzetta and Angelo L. Gobbi for supporting us with the photolithography and thin-film deposition processes for obtaining the platinum trails on glass slides. Elcio L. Pires, Mariane P. Pereira, Bruna P. M. Ramasini, Otavio Berenguel, and Carolina P. Torres are thanked for helping us with the SEM, LSCM, μCT, XPS, and Raman experiments, respectively. In addition, Iris R. Sousa Ribeiro is thanked for the support with the drawings. These professionals are from the Brazilian Center for Research in Energy and Materials. This work was sponsored by the Brazilian Coordination for Improvement of Higher Education Personnel (CAPES, grant 88881.504639/2020-01), the Brazilian National Council for Scientific and Technological Development (CNPq, grant 304389/2019-6), the São Paulo Research Foundation (FAPESP, grant 2017/02317-2), and the National Institute of Science and Technology in Bioanalytics (FAPESP grant 2014/50867-3 and CNPq grants 465389/2014-7 and 401256/2020-0).

■ REFERENCES

(1) Gooding, J. J.; Liu, S. M. A New Year Period Emphasizing the Need for Better Sensors. *ACS Sens.* **2020**, *5*, 597−598.

(2) Russo, M. J.; Han, M.; Desroches, P. E.; Manasa, C. S.; Dennaoui, J.; Quigley, A. F.; Kapsa, R. M. I.; Moulton, S. E.; Guijt, R. M.; Greene, G. W.; Silva, S. M. Antifouling Strategies for Electrochemical Biosensing: Mechanisms and Performance Toward

Point of Care Based Diagnostic Applications. *ACS Sens.* **2021**, *6*, 1482−1507.
(3) Labib, M.; Sargent, E. H.; Kelley, S. O. Electrochemical Methods for The Analysis of Clinically Relevant Biomolecules. *Chem. Rev.* **2016**, *116*, 9001−9090.
(4) Farka, Z.; Juřík, T.; Kovář, D.; Trnková, L.; Skládal, P. Nanoparticle-Based Immunochemical Biosensors and Assays: Recent Advances and Challenges. *Chem. Rev.* **2017**, *117*, 9973−10042.
(5) Cohen, L.; Walt, D. R. Highly Sensitive and Multiplexed Protein Measurements. *Chem. Rev.* **2019**, *119*, 293−321.
(6) Seo, G.; Lee, G.; Kim, M. J.; Baek, S.-H.; Choi, M.; Ku, K. B.; Lee, C.-S.; Jun, S.; Park, D.; Kim, H. G.; Kim, S.-J.; Lee, J.-O.; Kim, B. T.; Park, E. C.; Kim, S. I. Rapid Detection of COVID-19 Causative Virus (SARS-Cov-2) in Human Nasopharyngeal Swab Specimens Using Field-Effect Transistor-Based Biosensor. *ACS Nano* **2020**, *14*, 5135−5142.
(7) Shan, B.; Broza, Y. Y.; Li, W.; Wang, Y.; Wu, S.; Liu, Z.; Wang, J.; Gui, S.; Wang, L.; Zhang, Z.; Liu, W.; Zhou, S.; Jin, W.; Zhang, Q.; Hu, D.; Lin, L.; Zhang, Q.; Li, W.; Wang, J.; Liu, H.; Pan, Y.; Haick, H. Multiplexed Nanomaterial-Based Sensor Array for Detection of COVID-19 in Exhaled Breath. *ACS Nano* **2020**, *14*, 12125−12132.
(8) Zhao, H.; Liu, F.; Xie, W.; Zhou, T.-C.; OuYang, J.; Jin, L.; Li, H.; Zhao, C.-Y.; Zhang, L.; Wei, J.; Zhang, Y.-P.; Li, C.-P. Ultrasensitive Supersandwich-Type Electrochemical Sensor for SARS-Cov-2 from the Infected COVID-19 Patients Using a Smartphone. *Sens. Actuators, B* **2021**, *327*, 128899.
(9) Alafeef, M.; Dighe, K.; Moitra, P.; Pan, D. Rapid, Ultrasensitive, and Quantitative Detection of SARS-Cov-2 Using Antisense Oligonucleotides Directed Electrochemical Biosensor Chip. *ACS Nano* **2020**, *14*, 17028−17045.
(10) Sabaté Del Río, J.; Henry, O. Y. F.; Jolly, P.; Ingber, D. E. An Antifouling Coating That Enables Affinity-Based Electrochemical Biosensing in Complex Biological Fluids. *Nat. Nanotechnol.* **2019**, *14*, 1143−1149.
(11) Gooding, J. J. Finally, A Simple Solution to Biofouling. *Nat. Nanotechnol.* **2019**, *14*, 1089−1090.
(12) Jiang, C.; Wang, G.; Hein, R.; Liu, N.; Luo, X.; Davis, J. J. Antifouling Strategies for Selective In Vitro And In Vivo Sensing. *Chem. Rev.* **2020**, *120*, 3852−3889.
(13) Lin, P.-H.; Li, B.-R. Antifouling Strategies in Advanced Electrochemical Sensors and Biosensors. *Analyst* **2020**, *145*, 1110−1120.
(14) Campuzano, S.; Pedrero, M.; Yáñez-Sedeño, P.; Pingarrón, J. Antifouling (Bio)Materials for Electrochemical (Bio)Sensing. *Int. J. Mol. Sci.* **2019**, *20*, 423.
(15) Pelaz, B.; del Pino, P.; Maffre, P.; Hartmann, R.; Gallego, M.; Rivera-Fernández, S.; de la Fuente, J. M.; Nienhaus, G. U.; Parak, W. J. Surface Functionalization of Nanoparticles with Polyethylene Glycol: Effects on Protein Adsorption and Cellular Uptake. *ACS Nano* **2015**, *9*, 6996−7008.
(16) Lísalová, H.; Brynda, E.; Houska, M.; Víšová, I.; Mrkvová, K.; Song, X. C.; Gedeonová, E.; Surman, F.; Riedel, T.; Pop-Georgievski, O.; Homola, J. Ultralow-Fouling Behavior of Biorecognition Coatings Based on Carboxy-Functional Brushes of Zwitterionic Homo- and Copolymers in Blood Plasma: Functionalization Matters. *Anal. Chem.* **2017**, *89*, 3524−3531.
(17) Li, H.; Dauphin-Ducharme, P.; Arroyo-Currás, N.; Tran, C. H.; Vieira, P. A.; Li, S.; Shin, C.; Somerson, J.; Kippin, T. E.; Plaxco, K. W. A Biomimetic Phosphatidylcholine-Terminated Monolayer Greatly Improves the In Vivo Performance of Electrochemical Aptamer-Based Sensors. *Angew. Chem., Int. Ed.* **2017**, *56*, 7492−7495.
(18) Cui, M.; Wang, Y.; Jiao, M.; Jayachandran, S.; Wu, Y.; Fan, X.; Luo, X. Mixed Self-Assembled Aptamer and Newly Designed Zwitterionic Peptide as Antifouling Biosensing Interface for Electrochemical Detection of Alpha-Fetoprotein. *ACS Sens.* **2017**, *2*, 490−494.
(19) Dhanapala, L.; Jones, A. L.; Czarnecki, P.; Rusling, J. F. Sub-Zeptomole Detection of Biomarker Proteins Using a Microfluidic Immunoarray with Nanostructured Sensors. *Anal. Chem.* **2020**, *92*, 8021−8025.
(20) Lin, S.; Yu, W.; Wang, B.; Zhao, Y.; En, K.; Zhu, J.; Cheng, X.; Zhou, C.; Lin, H.; Wang, Z.; Hojaiji, H.; Yeung, C.; Milla, C.; Davis, R. W.; Emaminejad, S. Noninvasive wearable electroactive pharmaceutical monitoring for personalized therapeutics. *Proc. Natl. Acad. Sci. U.S.A.* **2020**, *117*, 19017−19025.
(21) Ye, T.-N.; Feng, W.-J.; Zhang, B.; Xu, M.; Lv, L.-B.; Su, J.; Wei, X.; Wang, K.-X.; Li, X.-H.; Chen, J.-S. Converting waste paper to multifunctional graphene-decorated carbon paper: from trash to treasure. *J. Mater. Chem. A* **2015**, *3*, 13926−13932.
(22) Duran, G. M.; Benavidez, T. E.; Giuliani, J. G.; Rios, A.; Garcia, C. D. Synthesis of Cunp-Modified Carbon Electrodes Obtained by Pyrolysis of Paper. *Sens. Actuators, B* **2016**, *227*, 626−633.
(23) Noviana, E.; Ozer, T.; Carrell, C. S.; Link, J. S.; McMahon, C.; Jang, I.; Henry, C. S. Microfluidic Paper-Based Analytical Devices: From Design to Applications. *Chem. Rev.* **2021**, *121*, 11835−11885.
(24) Shimizu, F. M.; Pasqualeti, A. M.; Nicoliche, C. Y. N.; Gobbi, A. L.; Santhiago, M.; Lima, R. S. Alcohol-Triggered Capillarity Through Porous Pyrolyzed Paper-Based Electrodes Enables Ultrasensitive Electrochemical Detection of Phosphate. *ACS Sens.* **2021**, *6*, 3125−3132.
(25) deAraujo, W. R.; Frasson, C. M. R.; Ameku, W. A.; Silva, J. R.; Angnes, L.; Paixão, T. R. L. C. Single -StepReagentless Laser Scribing Fabrication of Electrochemical Paper -BasedAnalytical Devices. *Angew. Chem. Int. Ed.* **2017**, *56*, 15113−15117.
(26) Silva, L. A. J.; da Silva, W. P.; Giuliani, J. G.; Canobre, S. C.; Garcia, C. D.; Munoz, R. A. A.; Richter, E. M. Use of Pyrolyzed Paper as Disposable Substrates for Voltammetric Determination of Trace Metals. *Talanta* **2017**, *165*, 33−38.
(27) Damasceno, S.; Corrêa, C. C.; Gouveia, R. F.; Strauss, M.; Bufon, C. C. B.; Santhiago, M. Delayed Capillary Flow of Elastomers: An Efficient Method for Fabrication and Nanofunctionalization of Flexible, Foldable, Twistable, And Stretchable Electrodes from Pyrolyzed Paper. *Adv. Electron. Mater.* **2020**, *6*, 1900826.
(28) Lima, R. S.; Strauss, M.; Santhiago, M. Flexible Carbon-Based Electrochemical Devices: Exploring the Three-Dimensional Architecture of Paper. *Reference Module in Biomedical Sciences*; Elsevier, 2021.
(29) Fingolo, A. C.; Bettini, J.; da Silva Cavalcante, M.; Pereira, M. P.; Bufon, C. C. B.; Santhiago, M.; Strauss, M. Boosting Electrical Conductivity of Sugarcane Cellulose and Lignin Biocarbons Through Annealing Under Isopropanol Vapor. *ACS Sustain. Chem. Eng.* **2020**, *8*, 7002−7010.
(30) Zhang, Z.; Orski, S.; Woys, A. M.; Yuan, G.; Zarraga, I. E.; Wagner, N. J.; Liu, Y. Adsorption of Polysorbate 20 And Proteins on Hydrophobic Polystyrene Surfaces Studied by Neutron Reflectometry. *Colloids Surf., B* **2018**, *168*, 94−102.
(31) Bharathi, S.; Nogami, M.; Ikeda, S. Novel Electrochemical Interfaces with A Tunable Kinetic Barrier by Self-Assembling Organically Modified Silica Gel and Gold Nanoparticles. *Langmuir* **2001**, *17*, 1−4.
(32) Wrapp, D.; Wang, N.; Corbett, K. S.; Goldsmith, J. A.; Hsieh, C.-L.; Abiona, O.; Graham, B. S.; Mclellan, J. S. Cryo-EM Structure of the 2019-Ncov Spike in the Prefusion Conformation. *Science* **2020**, *367*, 1260−1263.
(33) Kimling, J.; Maier, M.; Okenve, B.; Kotaidis, V.; Ballot, H.; Plech, A. Turkevich Method for Gold Nanoparticle Synthesis Revisited. *J. Phys. Chem. B* **2006**, *110*, 15700−15707.
(34) Hoffmann, C.; Blume, A.; Miller, I.; Garidel, P. Insights into protein-polysorbate interactions analysed by means of isothermal titration and differential scanning calorimetry. *Eur. Biophys. J.* **2009**, *38*, 557−568.
(35) Couston, R. G.; Skoda, M. W.; Uddin, S.; van der Walle, C. F. Adsorption Behavior of A Human Monoclonal Antibody at Hydrophilic and Hydrophobic Surfaces. *Mabs* **2013**, *5*, 126−139.
(36) Chen, R. J.; Bangsaruntip, S.; Drouvalakis, K. A.; Wong Shi Kam, N.; Shim, M.; Li, Y.; Kim, W.; Utz, P. J.; Dai, H. Noncovalent functionalization of carbon nanotubes for highly specific electronic biosensors. *Proc. Natl. Acad. Sci. U.S.A.* **2003**, *100*, 4984−4989.

https://doi.org/10.1021/acsami.1c18778
ACS Appl. Mater. Interfaces 2022, 14, 2522−2533

(37) So, H.-M.; Won, K.; Kim, Y. H.; Kim, B.-K.; Ryu, B. H.; Na, P. S.; Kim, H.; Lee, J.-O. Single-walled carbon nanotube biosensors using aptamers as molecular recognition elements. *J. Am. Chem. Soc.* **2005**, *127*, 11906−11907.
(38) Ostuni, E.; Chapman, R. G.; Holmlin, R. E.; Takayama, S.; Whitesides, G. M. A Survey of Structure−Property Relationships of Surfaces that Resist the Adsorption of Protein. *Langmuir* **2001**, *17*, 5605−5620.
(39) Siddiqui, S.; Arumugam, P. U.; Chen, H.; Li, J.; Meyyappan, M. Characterization of Carbon Nanofiber Electrode Arrays Using Electrochemical Impedance Spectroscopy: Effect of Scaling Down Electrode Size. *ACS Nano* **2010**, *4*, 955−961.
(40) Randviir, E. P. A cross examination of electron transfer rate constants for carbon screen-printed electrodes using Electrochemical Impedance Spectroscopy and cyclic voltammetry. *Electrochim. Acta* **2018**, *286*, 179−186.
(41) Graca, M.; Bongaerts, J. H. H.; Stokes, J. R.; Granick, S. Friction and Adsorption of Aqueous Polyoxyethylene (Tween) Surfactants at Hydrophobic Surfaces. *J. Colloid Interface Sci.* **2007**, *315*, 662−670.
(42) Nicoliche, C. Y. N.; Costa, G. F.; Gobbi, A. L.; Shimizu, F. M.; Lima, R. S. Pencil Graphite Core for Pattern Recognition Applications. *Chem. Commun.* **2019**, *55*, 4623−4626.
(43) McCrory, C. C. L.; Jung, S.; Peters, J. C.; Jaramillo, T. F. Benchmarking Heterogeneous Electrocatalysts for The Oxygen Evolution Reaction. *J. Am. Chem. Soc.* **2013**, *135*, 16977−16987.
(44) Ali, M. A.; Hu, C.; Jahan, S.; Yuan, B.; Saleh, M. S.; Ju, E.; Gao, S. J.; Panat, R. Sensing of COVID-19 Antibodies in Seconds via Aerosol Jet Nanoprinted Reduced-Graphene-Oxide-Coated 3D Electrodes. *Adv. Mater.* **2021**, *33*, 2006647.
(45) Udugama, B.; Kadhiresan, P.; Kozlowski, H. N.; Malekjahani, A.; Osborne, M.; Li, V. Y. C.; Chen, H.; Mubareka, S.; Gubbay, J. B.; Chan, W. C. W. Diagnosing COVID-19: The Disease and Tools for Detection. *ACS Nano* **2020**, *14*, 3822−3835.
(46) Liu, G.; Rusling, J. F. COVID-19 Antibody Tests and Their Limitations. *ACS Sens.* **2021**, *6*, 593−612.
(47) Younes, N.; Al-Sadeq, D. W.; Al-Jighefee, H.; Younes, S.; Al-Jamal, O.; Daas, H. I.; Yassine, H. M.; Nasrallah, G. K. Challenges in Laboratory Diagnosis of the Novel Coronavirus SARS-Cov-2. *Viruses* **2020**, *12*, 582.
(48) Guo, K.; Wustoni, S.; Koklu, A.; Díaz-Galicia, E.; Moser, M.; Hama, A.; Alqahtani, A. A.; Ahmad, A. N.; Alhamlan, F. S.; Shuaib, M.; Pain, A.; McCulloch, I.; Arold, S. T.; Grünberg, R.; Inal, S. Rapid Single-Molecule Detection of COVID-19 and MERS Antigens Via Nanobody-Functionalized Organic Electrochemical Transistors. *Nat. Biomed. Eng.* **2021**, *5*, 666−677.
(49) Kwon, O. S.; Song, H. S.; Park, T. H.; Jang, J. Conducting Nanomaterial Sensor Using Natural Receptors. *Chem. Rev.* **2019**, *119*, 36−93.
(50) Schroeder, V.; Savagatrup, S.; He, M.; Lin, S.; Swager, T. M. Carbon Nanotube Chemical Sensors. *Chem. Rev.* **2019**, *119*, 599−663.
(51) Garrote, B. L.; Santos, A.; Bueno, P. R. Perspectives on And Precautions for The Uses of Electric Spectroscopic Methods in Label-Free Biosensing Applications. *ACS Sens.* **2019**, *4*, 2216−2227.
(52) Beduk, T.; Beduk, D.; de Oliveira Filho, J. I.; Zihnioglu, F.; Cicek, C.; Sertoz, R.; Arda, B.; Goksel, T.; Turhan, K.; Salama, K. N.; Timur, S. Rapid Point-of-Care COVID-19 Diagnosis with a Gold-Nanoarchitecture-Assisted Laser-Scribed Graphene Biosensor. *Anal. Chem.* **2021**, *93*, 8585−8594.
(53) Piella, J.; Bastús, N. G.; Puntes, V. Size-Dependent Protein-Nanoparticle Interactions in Citrate-Stabilized Gold Nanoparticles: The Emergence of the Protein Corona. *Bioconjugate Chem.* **2017**, *28*, 88−97.
(54) Casals, E.; Pfaller, T.; Duschl, A.; Oostingh, G. J.; Puntes, V. Time Evolution of the Nanoparticle Protein Corona. *ACS Nano* **2010**, *4*, 3623−3632.

https://doi.org/10.1021/acsami.1c18778
ACS Appl. Mater. Interfaces 2022, 14, 2522−2533